Quantitative Evaluation of the Lunar Seismic Scattering and Comparison Between the Earth, Mars, and the Moon

Keisuke Onodera, Taichi Kawamura, Satoshi Tanaka, Yoshiaki Ishihara, Takuto Maeda

JGR Planets

RESEARCH ARTICLE
10.1029/2022JE007558

Key Points:

- Through full 3D seismic wave propagation simulation, we quantitatively evaluated the lunar seismic scattering properties
- We found that a 10-km thick scattering layer with 10% velocity fluctuation well-reproduced the Apollo seismic observation
- Our results show that the upper lunar crust is about 10 times more heterogeneous than that of the Earth and Mars

Supporting Information:

Supporting Information may be found in the online version of this article.

Correspondence to:

K. Onodera,
onodera@eri.u-tokyo.ac.jp

Citation:

Onodera, K., Kawamura, T., Tanaka, S., Ishihara, Y., & Maeda, T. (2022). Quantitative evaluation of the lunar seismic scattering and comparison between the Earth, Mars, and the Moon. *Journal of Geophysical Research: Planets*, *127*, e2022JE007558. https://doi.org/10.1029/2022JE007558

Received 2 SEP 2022
Accepted 1 DEC 2022

Author Contributions:

Conceptualization: Keisuke Onodera, Taichi Kawamura, Satoshi Tanaka, Yoshiaki Ishihara, Takuto Maeda
Data curation: Keisuke Onodera
Formal analysis: Keisuke Onodera
Investigation: Keisuke Onodera, Taichi Kawamura, Yoshiaki Ishihara, Takuto Maeda
Methodology: Keisuke Onodera, Taichi Kawamura, Yoshiaki Ishihara, Takuto Maeda
Resources: Keisuke Onodera
Software: Keisuke Onodera, Yoshiaki Ishihara
Supervision: Taichi Kawamura, Satoshi Tanaka
Validation: Keisuke Onodera, Taichi Kawamura, Satoshi Tanaka
Visualization: Keisuke Onodera

Quantitative Evaluation of the Lunar Seismic Scattering and Comparison Between the Earth, Mars, and the Moon

Keisuke Onodera[1,2,3], Taichi Kawamura[2], Satoshi Tanaka[3,4], Yoshiaki Ishihara[5], and Takuto Maeda[6]

[1]Earthquake Research Institute, The University of Tokyo, Tokyo, Japan, [2]Université Paris Cité, Institut de Physique du Globe de Paris, CNRS, Paris, France, [3]Department of Space and Astronautical Sciences, The Graduate University for Advanced Studies, SOKENDAI, Hayama, Japan, [4]Institute of Space and Astronautical Science, Japan Aerospace Exploration Agency, Sagamihara, Japan, [5]JAXA Space Exploration Center (JSEC), Japan Aerospace Exploration Agency, Sagamihara, Japan, [6]Graduate School of Science and Technology, Hirosaki University, Hirosaki-shi, Japan

Abstract The intense seismic scattering seen in Apollo lunar seismic data is one of the most characteristic features, making the seismic signals much different from those observed on the Earth. The scattering is considered to be attributed to subsurface heterogeneity. While the heterogeneous structure of the Moon reflects the past geological activities and evolution processes from the formation, the detailed description remains an open issue. Here, we present a new model of the subsurface heterogeneity within the upper lunar crust derived through a full 3D seismic wave propagation simulation. Our simulation successfully reproduced the Apollo seismic observations, leading to a significant update of the scattering properties of the Moon. The results showed that the scattering intensity of the Moon is about 10 times higher than that of the heterogeneous region on the Earth. The quantified scattering parameters could give us a constraint on the surface evolution process of the Moon and enable the comparative study for answering a fundamental question of why the seismological features are different on various planetary bodies.

Plain Language Summary In the past Apollo missions, several seismometers were installed on the nearside of the Moon and they brought us the first seismic records from an extraterrestrial body. The derived lunar seismic data surprised us because of their extremely long duration (1–2 hr) and spindle-shaped form, which were barely observed on Earth. These characteristics, which are different from earthquakes, are thought to reflect the subsurface heterogeneity. However, the inhomogeneous structure within the lunar crust is poorly constrained. To improve our knowledge of wave propagation on an extraterrestrial body, this study evaluated the subsurface heterogeneity through 3D seismic wave propagation simulation. After running some simulations under various structure settings, we found that a certain set of parameters well reproduced the Apollo seismic data, resulting in a new heterogeneous structure model of the Moon. The evaluated parameters were compared with those measured on the Earth and Mars, and we found that the Moon is more heterogeneous than others by about 10 times. This kind of comparison makes it easier to interpret the observed seismic signals on each solid body. Also, it is useful to explain the differences in their surface evolution scenarios. We believe that our results contribute to further extending comparative planetology.

1. Introduction

The intensely scattered seismic waves with a long duration (1–2 hr) and ambiguous phase arrivals (e.g., P and S) are one of the characteristics observed in the Apollo lunar seismic data (Latham et al., 1970; Figure 1a). According to the previous studies on Earth, it is considered that this feature is ascribed to subsurface heterogeneities such as cracks, igneous intrusions, and faults (Sato et al., 2012 and references therein). While intense scattering is the essence of lunar seismic signals, its properties are not fully understood.

In general, estimating the planetary interior using seismic waves relies on precise phase identifications (e.g., P and S arrivals). Yet, the extremely high scattering environment on the Moon makes it more challenging to pick up the phases, leading to considerable uncertainty in the resultant structure model (e.g., Garcia et al., 2019). Thus, it can be said that the scattering is an essential characteristic of the lunar seismic waves, whereas it is the most severe obstacle for the investigation of the lunar internal structure. Moreover, the seismic data from Mars also show intensely scattered features (e.g., Lognonné et al., 2020; Menina et al., 2021), implying that seismic scattering is not just a specific problem in lunar seismology but also a common problem in planetary seismology.

Writing – original draft: Keisuke Onodera
Writing – review & editing: Keisuke Onodera, Taichi Kawamura, Satoshi Tanaka, Takuto Maeda

Therefore, it is valuable to push forward our understanding of this topic for elucidating the nature of seismic wave propagation on extraterrestrial bodies.

In seismology, there are two important parameters to explain seismic energy decay. The first one is termed as "scattering attenuation"—energy loss due to heterogeneity or scatterer—and the second is called "intrinsic attenuation"—energy loss due to the absorption by a medium. To retrieve these parameters, radiative transfer theory (e.g., Aki, 1969; Aki & Chouet, 1975; Sato, 1977; Wu, 1985) has been used on the Earth and applied to the Moon and Mars (e.g., Dainty & Toksöz, 1981; Dainty et al., 1974; Menina et al., 2021; Karakostas et al., 2021). In this theory, there are three fundamental situations considered; single scattering (weak scattering), multiple scattering (intense scattering), and diffusion (extremely intense scattering). The single and multiple scattering conditions are widely applied to earthquakes and also marsquakes (e.g., Aki & Chouet, 1975; Menina et al., 2021), where we can confirm the clear P or S arrival onsets in seismic records (Figure 1b). On the other hand, under extremely intense scattering conditions like the Moon, the diffusion model is preferable (e.g., Dainty et al., 1974), where the seismic phases are well scattered and the waveform shows a spindle shape (Figure 1a).

For the Moon, the past studies (e.g., Blanchette-Guertin et al., 2012) mainly focused on the energy decay part to evaluate the intrinsic and scattering attenuation. In general, it is challenging to individually assess each contribution, hence the combined effects were obtained. On the other side, the energy growth part (i.e., from the first arrival to the energy peak arrival) reflects forward scattering effects, allowing us to evaluate the scattering attenuation more precisely. In fact, Dainty et al. (1974) tried to model the moonquake signals with the diffusion model. While the model well explained the decay part, an energy excess at the energy growth part was observed. This indicates that the diffusion model is not fully capable of explaining the lunar seismic signals, and another approach is required to better understand the scattering effect.

In this study, by employing a more straightforward way than before, we quantitatively evaluate the lunar scattering properties, which have remained an open and severe issue since lunar seismology started. Here, we conduct the first full 3D simulation of seismic wave propagation in this field. The advantage of numerical simulation is that it can consider more complicated problems (or more realistic conditions) while we are forced to assume a simple situation in analytical modeling. By performing the full 3D simulation, we investigated the lunar scattering effect under the most realistic condition ever considered before. In fact, the 3D simulation costs an extremely large amount of computational resources and limits us to computing only a few hundred of seconds' time series. However, our high spatiotemporal resolution simulation enables us to better model the energy growth part, allowing us to evaluate the scattering attenuation effect more precisely than previous approaches.

In the following sections, we present the fundamental idea of the 3D seismic wave propagation simulation and how to compare the simulated results with the observation. Then, we show the results and discuss the obtained scattering structure within the lunar crust together with the previously proposed models. Finally, we compare our results with the Earth and Mars, and discuss why we observe different seismological features on each solid body. Since this kind of comparative study helps us infer how the evolution processes differ among solid planetary bodies, we believe that our results will not just contribute to deepening our understanding of lunar science but also pushing forward comparative planetology.

2. Methodology

The previous works (e.g., Dainty & Toksöz, 1981; Gillet et al., 2017) inverted scattering and attenuation parameters such as scattering quality factor (Q_s) and intrinsic quality factor (Q_i) based on the radiative transfer theory. In the theory, it is considered how incident wave loses the energy due to scattering media and how the shape of energy envelope varies depending on the intensity of heterogeneity (e.g., Sato et al., 2012). Under the intense heterogeneity, this approach works well to explain the decay coda, which strongly reflects the intrinsic attenuation—the energy absorption by medium (e.g., Lognonné et al., 2020). Whereas, the theory is not fully capable of modeling the energy growth part, where the scattering effects are more dominant (Figure 1a). To overcome this problem, we performed forward modeling with 3D seismic wave propagation simulation, including all possible scattering sources such as topographies and wave velocity fluctuation, so to speak, full 3D simulation. The idea is to perform wave propagation simulations under various settings and to find a set of parameters that can well-reproduce the observations. While such an approach was known to be the most straightforward way to evaluate the scattering environment, it was unrealistic to take this approach because it requires a vast amount of computational resources.

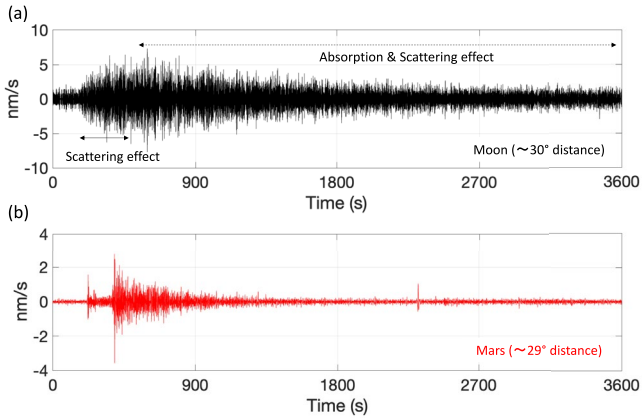

Figure 1. (a) An example of a lunar seismic wave. The horizontal axis shows time in seconds and the vertical shows the velocity in nm/s. This is an impact-induced event recorded on December 15 in 1974 with the vertical component of the long-period seismometer installed at the Apollo 15 landing site. The waveform is band-pass filtered between 0.3 and 1.5 Hz. This event is estimated to have occurred about 30° away from the Apollo 15 station (Oberst, 1989). (b) An example of marsquake (S235b). This event was observed on July 26 in 2019 by InSight (Interior Exploration using Seismic Investigations, Geodesy, and Heat Transport) on Mars. The waveform is band-pass filtered between 0.1 and 0.8 Hz. The epicentral distance is about 29° (InSight Mars SEIS data Service, 2019).

Recently, accompanied by the significant progress in computational technology, it is now possible to perform the forward approach. In this study, utilizing one of the best supercomputers existing (Earth Simulator fourth generation of Japan Agency for Marine-Earth Science and Technology), we performed the first full 3D simulation in lunar seismology to constrain the scattering properties more directly. In this section, we summarize the key points of the numerical simulation.

2.1. Simulation Code for 3D Seismic Wave Propagation

We used the Open-source Seismic Wave Propagation Code (OpenSWPC) developed by Maeda et al. (2017), which is based on the finite difference method with heterogeneity, oceanic layer, and topography (HOT-FDM; Nakamura et al., 2012). The code enables us to include both lunar topographies and scattering media that are mandatory functionalities in this study. Another point is that we realized a stable computation up to 2 Hz, which covers the peak sensitivity frequency band of the Apollo long period (LP) seismometer (0.3–1.5 Hz), realizing the first direct comparison between the synthetics and the Apollo data at the same frequency range.

2.2. Reference Events and Work Space

Since this work is the first attempt at full 3D simulation in this field, it is reasonable to start with the artificial impacts because of their well-constrained source locations, origin times, and impact parameters (e.g., kinetic energy and impact angle). Following Onodera et al. (2021) who performed a 2D simulation of the lunar seismic wave propagation, we adopted two Saturn IVB rocket booster impacts (SIVB impacts): Apollo 16 SIVB and Apollo 14 SIVB impacts recorded at Apollo 12 station (Figure 2a). The computational space for each event is shown in Figures 2b and 2c. The detailed configuration of the simulation is summarized in Text S1 and Table S4 in Supporting Information S1.

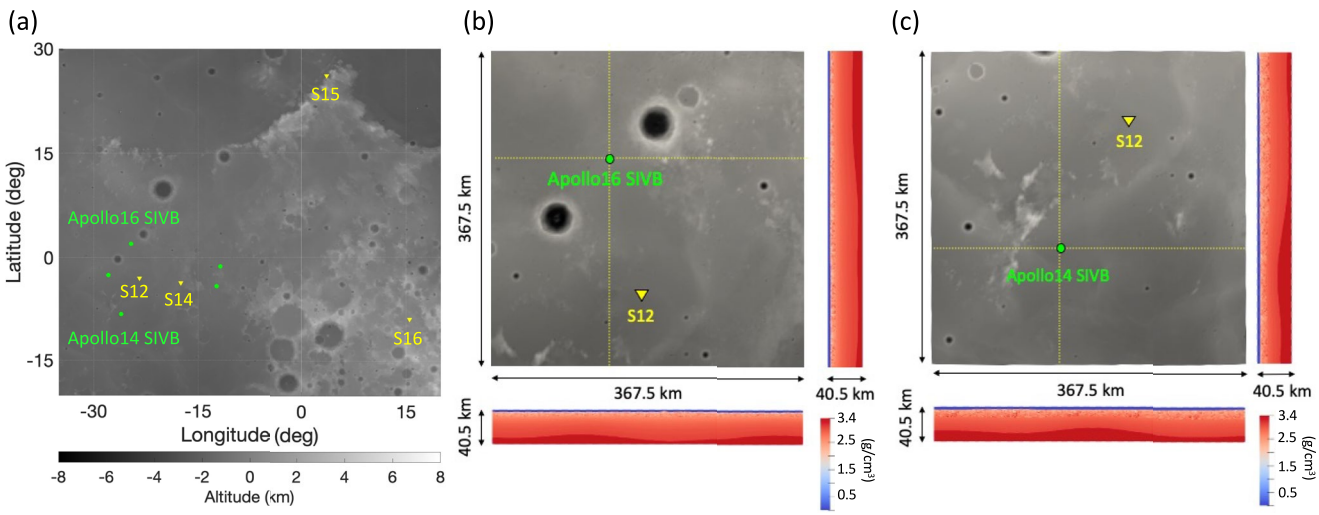

Figure 2. (a) Locations of Apollo SIVB impacts and seismic stations. The yellow inverse triangles show the locations of the Apollo seismometers and the green circles show the impact locations of the Apollo SIVB rocket boosters. The background is the digital elevation model (DEM) of the SELENE (Kaguya) laser altimeter (Araki et al., 2009). (b) Workspace for the 3D simulation of the Apollo 16 SIVB impact. The bottom and right-hand side panels display the cross-sections of E–W and N–S directions along with the yellow dotted lines. The grayscale corresponds to the surface topography (SLDEM2015; Barker et al., 2016) and the colored scale shows the density within the crust and mantle. The Moho boundary is inserted by referring the GRAIL (Gravity Recovery and Interior Laboratory) crustal model by Wieczorek et al. (2013). Note that the first several km includes random media (i.e., the density fluctuation). (c) Workspace for the 3D simulation of the Apollo 14 SIVB impact. The color scales and each panel are the same as in (b).

2.3. Velocity Structure

In constructing the velocity model, we considered the gravity data from the Gravity Recovery and Interior Laboratory (GRAIL) mission and the measurements of Apollo returned samples.

Regarding the density structure estimated from the GRAIL data, we used the density and porosity model provided by Besserer et al. (2014). Following their model, the density profile as a function of depth $\rho(z)$ can be written as follows:

$$\rho(z) = \rho_{\text{surf}} + \Delta\rho\left(1 - e^{-z/d}\right) \tag{1}$$

where, ρ_{surf} is the surface density, $\Delta\rho$ is the density contrast between fractured surface materials, and unfractured bedrock, and d is the e-folding depth. At the Apollo 12 landing region, these parameters take the values of 2,308 kg/m^3, 786 kg/m^3, and 9.8 km, respectively. The porosity as a function of depth $\phi(z)$ can be expressed as follows:

$$\phi(z) = 1 - \rho(z)/\rho_0 \tag{2}$$

where, $\rho_0 = \rho_{\text{surf}} + \Delta\rho$. Substituting Equation 1 into Equation 2 gives us the following:

$$\phi(z) = 1 - \frac{1}{\rho_{\text{surf}} + \Delta\rho}\left[\rho_{\text{surf}} + \Delta\rho\left(1 - e^{-\frac{z}{d}}\right)\right]. \tag{3}$$

In terms of the laboratory measurements, we referred an experimental work by Sondergeld et al. (1979). They constructed an empirical model of the compressional wave velocity $v_p(z)$ based on the measurements of the lunar anorthosite (Apollo sample: #60025, 174) as given below:

$$v_p(z) = \frac{v_{p0}}{\sqrt{1 - \phi(z)}}\exp\left[\frac{\left(\phi(z)^2 - \xi\right)\phi(z)}{2(1 - \phi(z))}\right] \tag{4}$$

where, v_{p0} (=7.15 km/s) is the P-wave velocity extrapolated from high pressure to zero pressure based on the results by Mizutani and Osako (1974). ξ is an empirical constant and the value ranges from 2 to 24, covering almost all velocity structure models proposed by the previous works (Besserer et al., 2014; Sondergeld et al., 1979). In other words, $\xi = 2$ gives the upper limit of the P-wave velocity structure while $\xi = 24$ does the lower limit (Figure 3a). Combining Equation 3 with the empirical velocity structure by Sondergeld et al. (1979) results in the reference model used in the simulations. We employed $\xi = 7$ based on the travel times computed for respective artificial impacts. See Texts S2 and S3 in Supporting Information S1 for the determination of ξ parameter and additional information about topography and velocity models.

Figure 3a shows the constructed P-wave velocity model. The model consists of three parts: megaregolith (the fragmented structure due to meteoroid impacts), crust, and mantle from top to bottom. It is worth noting that the random media, whose thickness varies from 3.5 to 10 km in the simulation, are inserted in the megaregolith layer. We will explain the scattering layer in the next section. With regards to the V_p/V_s ratio, Lognonné et al. (2003) and Gagnepain-Beyneix et al. (2006) suggested that it could range from 1.7 to 2.0 for high fractured materials. Also, Garcia et al. (2011) employed 2.0 for the top low-velocity layer. In this study, following the previous results, the value in the scattering layer is assumed to be 2.0. Concerning the consolidated layer, $\sqrt{3}$ is given for V_p/V_s. The intrinsic Q used in the simulation was provided combining the results by Nakamura and Koyama (1982) and Blanchette-Guertin et al. (2012) (Table S1 in Supporting Information S1).

2.4. Scattering Model

In terrestrial seismology, the behaviors of seismic scattering have been measured by both laboratory experiments and data analyses of seismic signals (e.g., Sato & Fehler, 1998; Sato et al., 2012; Sivaji et al., 2002). To quantitatively evaluate the properties of seismic scattering due to the heterogeneity inside a medium, previous works investigated the distribution of perturbation from an average velocity and expressed it in a mathematical way using the autocorrelation function (ACF) or power spectral density function (PSDF) (e.g., Sato & Fehler, 1998; Shiomi et al., 1997). According to Sato et al. (2012), there are a few types of ACFs: Gaussian, von Karman, and

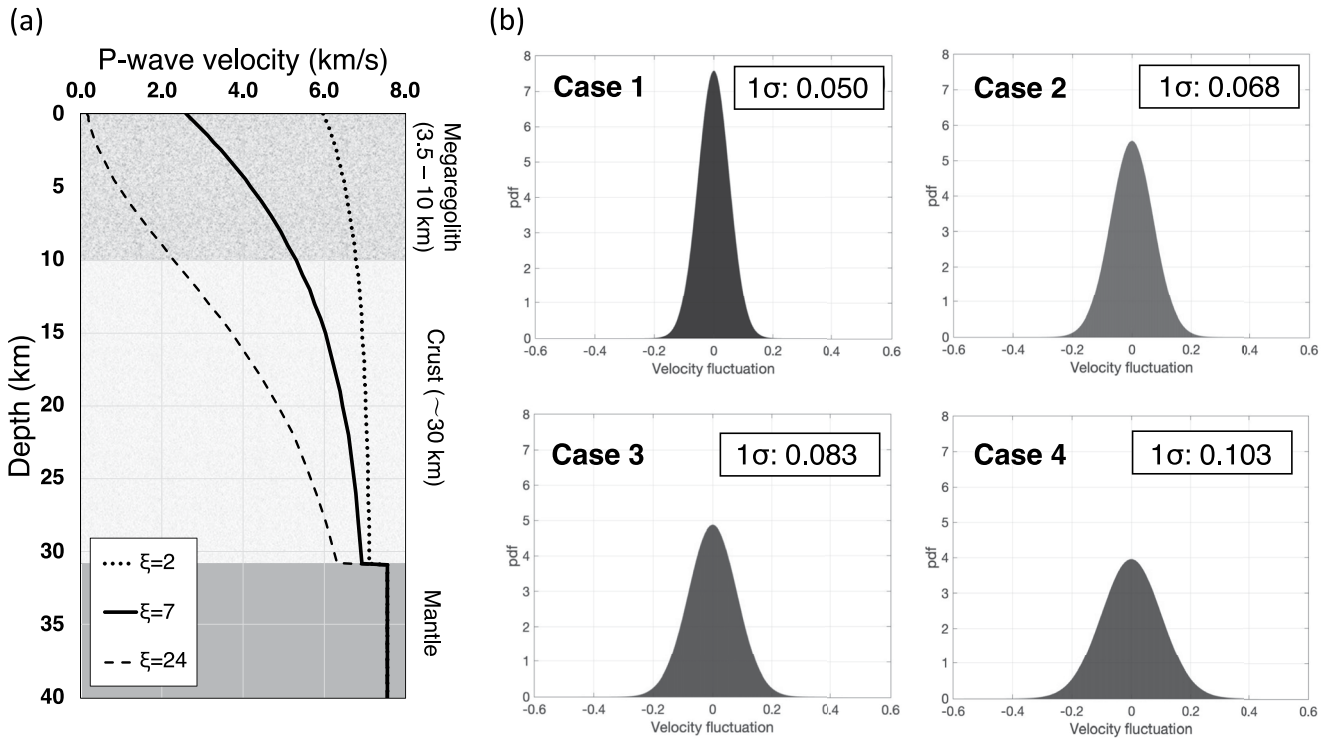

Figure 3. (a) Assumed velocity structure for the simulations. $\xi = 7$ was employed in this work. The structure consists of three parts: megaregolith, crust, and mantle. The random media is inserted into the megaregolith layer. The thickness of the layer varied from 3.5 to 10 km in the simulation. (b) Probability density distribution of the velocity fluctuation of the representative random media used in this study. As the 1σ of the fluctuation gets larger, the scattering effect becomes stronger.

Exponential. Among these, von Karman or Exponential is usually adopted in the seismological approaches (e.g., Shiomi et al., 1997; Sivaji et al., 2002; Suzuki et al., 1981). We assumed exponential ACF, which is a specific case of von Karman ACF. It is defined as follows:

$$R(r) = \varepsilon^2 \exp\left(-\frac{r}{a}\right) \tag{5}$$

where, r is lag distance, a is correlation length—the characteristic scale of the heterogeneity within a certain medium, and ε is fractional fluctuation which determines the velocity perturbation from the mean velocity structure.

To simulate the megaregolith (i.e., fragmented rocks by meteoroid impacts), we assumed the isotropic random media, where the correlation length in each direction takes the same value (i.e., $a_x = a_y = a_z$), and varied the fractional fluctuation ε from 0.024 to 0.042, corresponding to the 1σ of the velocity fluctuation from 5% to 10%.

Here, we focus on the four cases, where the typical scale of random media is fixed to 650 m and 1σ of the velocity fluctuation ranges from 5% to 10% (Figure 3b). The larger perturbation corresponds to more intense scattering (i.e., the scattering effects get stronger from Case 1 to Case 4). The parameter study about the correlation length is presented in Text S4 in Supporting Information S1.

Note that these parameters are for the initial runs to find preferable settings before the further detailed constraints. The additional scattering structure is presented in Section 3.3.

2.5. Source Model

As a source model for impacts, there are two approximations; one is the isotropic radiation with moment tensor and the other is the point force (or body force) expressed with the impulse. In past studies, either model was used to simulate the impact-induced seismic waves (e.g., Blanchette-Guertin et al., 2015; Daubar et al., 2020; Onodera et al., 2021). Since the detailed description of the impacts in terms of seismic source modeling is still an open

issue, we employed the simplest model—isotropic radiation. In fact, under the intense scattering structure as considered in this study, the radiation information is lost just after the energy is released, and the difference in the source model does not so much affect the resultant waveform (i.e., the structure is much more dominant to characterize the seismogram in this case). Readers can find more details of the source assumption in Text S5 in Supporting Information S1.

Besides, in the case of impacts, it is known that there are the shock regime—where plastic deformation occurs and the elastic regime—where the seismic wave starts to propagate. According to Rajšić et al. (2021), the transition from the shock regime into the elastic regime occurs about 0.15 km away from the Apollo SIVB impact location, which is a much smaller distance than the epicentral distance considered in this study (>150 km). Thereby, assuming there is little influence of the shock regime on our results, we pay attention to the elastic regime.

Also, it is worth noting that, through the subsequent simulations, we found that $(1.5 \pm 0.5) \times 10^{12}$ Nm is preferable as the seismic moment, which is equivalent to the seismic energy of $(5.5 \pm 1.8) \times 10^{6}$ J following Teanby and Wookey (2011). This leads to the seismic efficiency of $(1.2 \pm 0.4) \times 10^{-4}$. Because this is one of the least constrained parameters, we leave a brief note here for future impact physics works.

2.6. Quantitative Comparison Between Synthetics and Apollo Data

2.6.1. Preprocessing

First, as generally done in the seismological analysis, a long-term trend is removed from the raw Apollo seismic data. Concerning pre-filtering, the 4-th order Butterworth filter is applied with the cut-off frequency being 0.05 and 3.0 Hz. After that, we applied the Tukey window function with the lobe width being 3% of the data length. Then, the instrumental response of the Apollo LP peaked mode was corrected, which gave us the velocity time series data. In the end, we performed the post band-pass filtering around the peak sensitivity of the LP sensor in peaked mode (0.3–1.5 Hz).

Because of the radio-tracking of the artificial impacts, the source locations are well-constrained (Tables S2 and S3 in Supporting Information S1), which enables us to obtain the radial and transverse components using the azimuth information. Note that the seismometer was not aligned in a usual way for Apollo 12, that is, the positive direction of LPX (X component of LP sensor) is oriented toward 180°N and that of LPY (Y component of LP sensor) is toward 270°E.

2.6.2. Estimation of Rise-Time

As pointed out by Gillet et al. (2017) and Onodera et al. (2021), the energy growth part contains the information of the forward scattering while the decay-coda (i.e., from the peak energy to noise floor) more reflects the diffusion and intrinsic attenuation. Since this study focuses on the forward scattering effects, we paid closer attention to the energy growth part. In the following analysis, a parameter called "rise-time"—the time to reach the energy peak from the first arrival—is mainly used. Like P or S arrival reading, the rise-time is determined manually (e.g., Onodera et al., 2021). In the case of the Moon, it is estimated by taking a moving average of the seismic records and detecting the point where the gradient of energy increase becomes flat. In this work, all the seismic signals were smoothed with a window of 200 data points (~30 s). That means the uncertainty of the rise-time corresponds to ±15 s.

2.6.3. Equivalent Energy Density

We looked into the envelope shape in order to track the energy trend in time, which helps us assess how identical the synthetic data are compared to the real one. The seismic energy is proportional to the squared amplitude. Thereby, the equivalent energy E_{eq} is given by the following equation:

$$E_{\mathrm{eqi}} = \sum V_i^2(t)\,(i = R, T, Z) \tag{6}$$

where, $V(t)$ is the time-series of velocity signal for the radial, transverse, and vertical components. Since this study aims to see how the energy develops with time, we divided the time series into some sections and evaluate

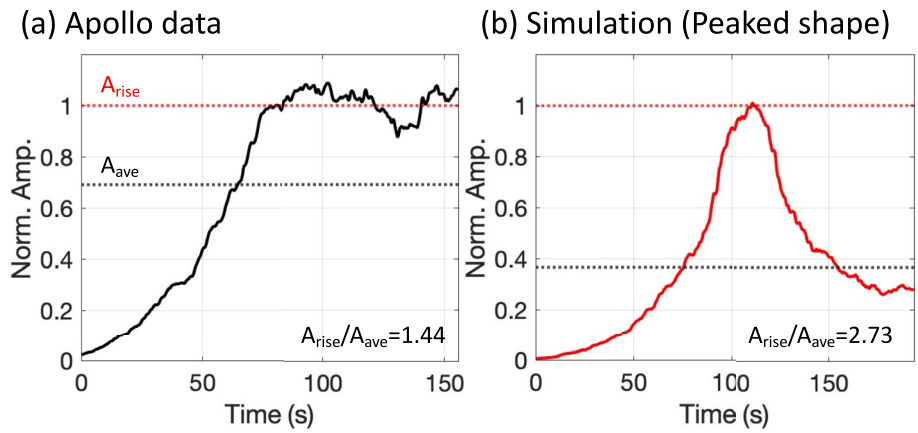

Figure 4. Examples of the amplitude ratio for (a) Apollo data and (b) simulation (Case1). A_{rise} is the amplitude at the rise-time, and A_{ave} stands for the average amplitude between arrivals to $2T_{\mathrm{rise}}$.

the energy density in a certain section instead of computing the total energy. Here, we introduce a new parameter called "equivalent energy density (EED)" E_d defined as follows:

$$E_{d_j} = \frac{1}{\tau_{j+1} - \tau_j} \sum_{t=\tau_{j+1}}^{\tau_{j+1}} V_i^2(t) \ (i = Z, R, T; j = 1, 2, \ldots, 2N_{\mathrm{div}} - 1) \tag{7}$$

$$\tau_n = \frac{nT_{\mathrm{rise}}}{N_{\mathrm{div}}} \ (n = 1, 2, \ldots, 2N_{\mathrm{div}})$$

where, T_{rise} shows the rise-time, and N_{div} (=10 in this study) determines how many sections the time series is divided into. Thereby, the E_d tells us how much energy is received at a station for a certain period, which is useful to track how the energy develops with time.

2.6.4. Amplitude Ratio

As another quantitative criterion, we evaluated how much the amplitude at the rise-time A_{rise} differs from the mean amplitude A_{ave}. Figure 4 shows two different cases. The typical lunar seismic signal represents a relatively flat feature after reaching the rise-time, which results in the $A_{\mathrm{rise}}/A_{\mathrm{ave}}$ ratio of ~1.4 (Figure 4a). Note that the time window between the first arrival and $2T_{\mathrm{rise}}$ is used to compute the average value. On the other hand, if a signal has a strong peak as in Figure 4b, the ratio takes a higher value.

3. Evaluation of Scattering Property Around the Apollo 12 Landing Site

As only two events are available in this study, the procedure is as follows: (a) constraining the scattering structure for the closer event (Apollo 16 SIVB impact), then (b) applying the structure to another event (Apollo 14 SIVB impact) to see whether the same structure can explain both observations. Unless the structure worked well for both events, a revision in the scattering structure would be given to minimize the discrepancy between synthetics and the data. Section 3.1 shows the results of rise-time, energy trend, and envelope shape for Apollo 16 SIVB impact observed at Station 12. Section 3.2 explains whether the structure based on the Apollo 16 SIVB event also works for Apollo 14 SIVB, and Section 3.3 describes how to improve the scattering structure to better explain both events.

3.1. The Initial Simulation Results for Apollo 16 SIVB Impact

Some examples of the simulation outputs are displayed in Figure 5, including snapshots of the horizontal plane (Figure 5a) and the comparison of smoothed energy envelopes for the vertical component between the Apollo (black profile) and synthetics (colored profile) (Figure 5b). Keep in mind that we present the case without scatterer (i.e., only topographies and layered structure are considered) for the comparison in the top row. The snapshots show the time evolution of wave propagation where the red wave shows the compressional component and

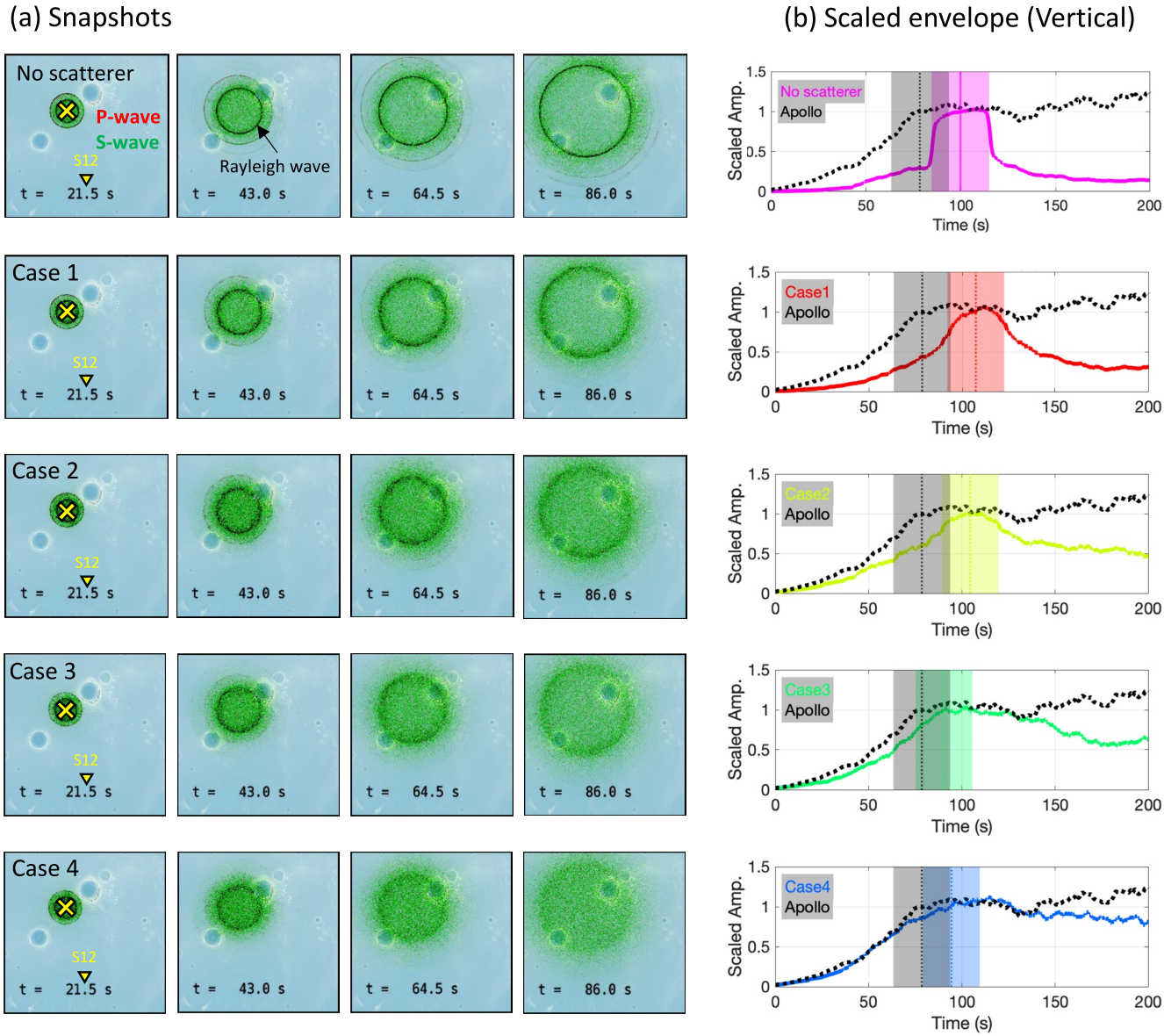

Figure 5. (a) Snapshots of each simulation on the horizontal plane. The time evolutions of wave propagation for Case 1 through Case 4 are shown from the second row to the bottom. Note that the simulation result without random media is shown at the top as a reference. The yellow cross shows the location of the source (Apollo 16 SIVB impact) and the seismic station (Station 12). The red wave corresponds to the compressional component and the green to the shear component. In this case, the random media displayed in Figure 3b are inserted in the first 5 km. The snapshots for the vertical cross sections are found in Figure S5 through Figure S9 in Supporting Information S1. Note that the absorption layer (Perfectly Matched Layer; Zhang & Shen, 2010) is inserted at the boundary to suppress artificial reflections. An example of snapshots for longer duration can be found in Figure S10 in Supporting Information S1. (b) Comparison of smoothed envelopes of the vertical component between the Apollo and synthetics for the respective cases. All results are filtered between 0.3 and 1.5 Hz, then smoothed with a 30 s time window and 50% overlap. The black curve corresponds to the Apollo data and the colored ones to the synthetics. The vertical lines with shade represent the peak energy (rise-time) arrivals and their error ranges. The error bar follows the window size for smoothing. The amplitudes are normalized with the value at the respective rise-times.

the green does the shear component. The black circle pattern corresponds to Rayleigh wave (e.g., the second panel in the first row of Figure 5a), which cannot be confirmed in the Apollo data. Thus, one of the important constraints in reproducing the Apollo observation is to attenuate the Rayleigh wave energy to the level of scattered body wave energy. Comparing the four scattering models, it is obvious that the stronger scattering (e.g., Case 4) diffuses the Rayleigh wave energy more rapidly compared to the weaker ones (e.g., Case 1) (Figure 5a). This difference can also be seen in the synthetic envelopes (Figure 5b). While the synthetic envelope shows a strong peak of the Rayleigh wave in the weak scattering condition (Case 1), as the scattering becomes more intense (Case 4), the Rayleigh wave energy is attenuated and the envelope shape gets more similar to the observation.

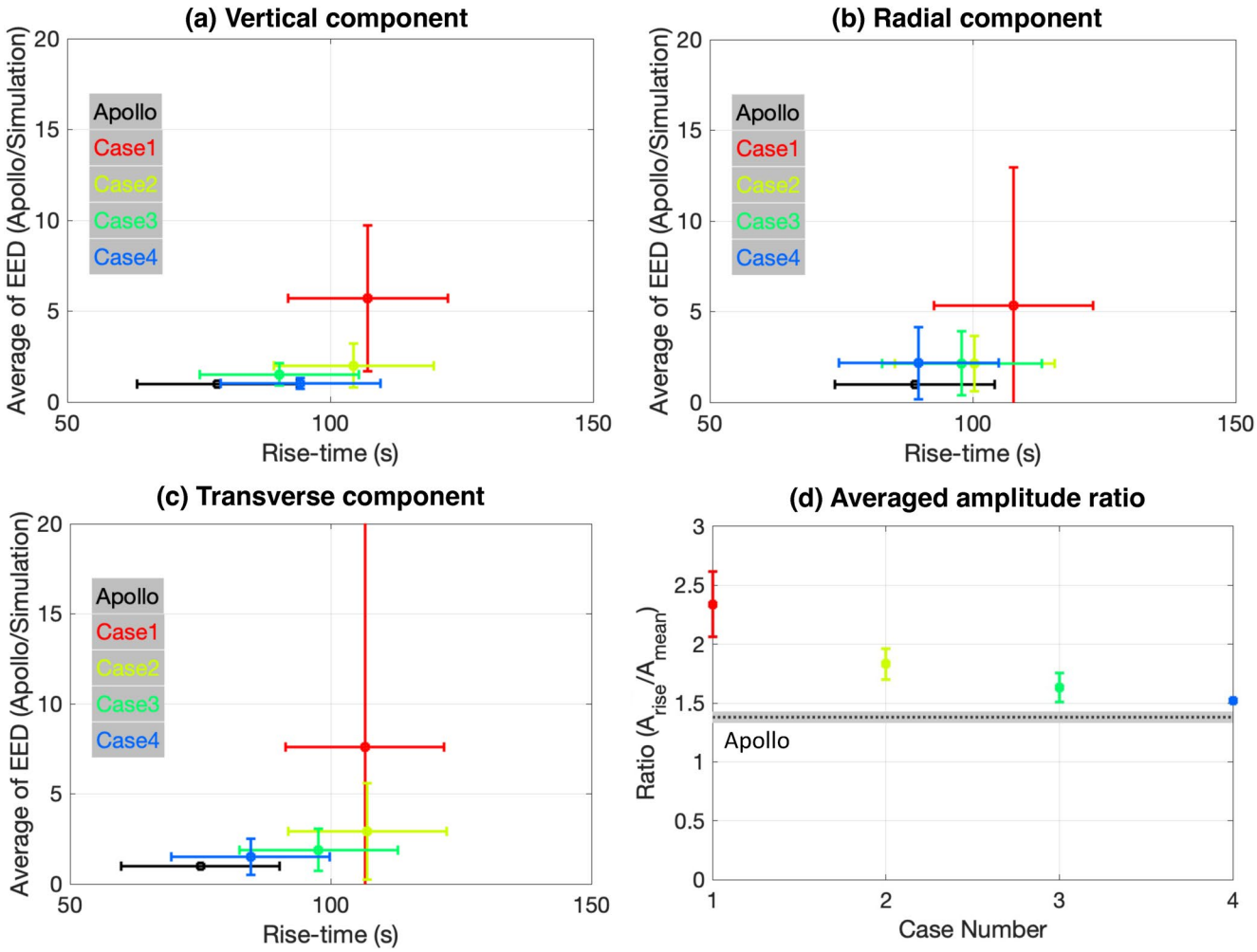

Figure 6. Rise-time versus equivalent energy density ratio (EED ratio) for (a) the vertical, (b) the radial, and (c) the transverse components. The black plots show the Apollo, and the colored are for respective simulation cases. The horizontal axis shows the rise-time with error of ±15 s. The vertical axis shows the average value of the EED ratio between the observation and synthetics over $2T_{rise}$ with standard deviation. (d) Results of the amplitude ratio values. The colored plots with error bars show the averaged values of the vertical, radial, and transverse components. The black dotted lines are the amplitude ratio values for the Apollo data with error range.

More quantitative comparison between the observations and synthetics was made by measuring the rise-time and EED (Figures 6a–6c). While Cases 1 and 2 are plotted far away from the Apollo, the intense scattering cases (Case 3 and 4) are in accordance with the observation. Moreover, looking at the results of the amplitude ratio (Figure 6d), we clearly observe that the ratio gets closer to the observation as the scattering gets stronger—meaning that the envelope shape changes from peaked-shape to flat one as seen in Figure 5b. From these results, we conclude Case 4 is preferable as a base model for the further investigations in the following sections.

3.2. Application of the Estimated Scattering Model to Apollo 14 SIVB Impact

To observe whether Case 4—the best model for the Apollo 16 SIVB impact—can also explain the other event, we performed another simulation for the Apollo 14 SIVB impact under the same parameter settings. Figure 7 compares the simulated envelopes with the Apollo ones. Overall, the envelope shape shows similar features to the data. The rise-time is in accordance with the error range for all components, and the amplitude ratio averaged using the three components takes the value of 1.59 ± 0.10 close to that of the Apollo (1.30 ± 0.05). However, making a comparison with the Case 4 results for the Apollo 16 SIVB impact (i.e., Figures 5b and 7a), it does not seem that the fitting and the consistency of energy trend is as good as that for the Apollo 16 SIVB case. In the following section, we give some modifications to the Case 4 structure to see what kind of model can improve the results.

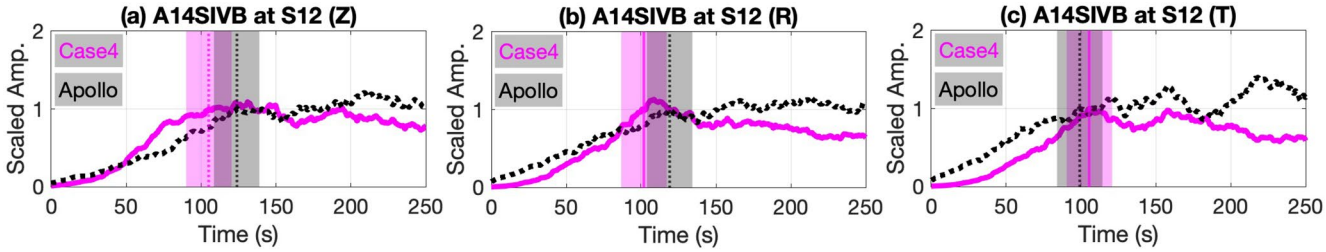

Figure 7. Smoothed envelopes of Apollo 14 SIVB impact observed at Station 12 in (a) the vertical, (b) the radial, and (c) the transverse components. The black envelopes are for the Apollo data, and the magenta profiles are for the simulation assuming Case 4 structure. The vertical lines with shade show the rise-time arrivals with error ranges. All envelopes are normalized with the value at each rise-time.

3.3. Modification of the Vertical Scattering Structure

To improve the simulation results for the Apollo 14 SIVB impact case, we modify the vertical scattering structure. Since the computation is expensive (28 TB total memory for each run), we prepared three different structures to roughly confirm what kind of structure improves the synthetics. The assumed structures (Case 4α, β, and γ) are shown in Figure 8a. Among these models, Case 4α shows a gradual decrease in velocity fluctuation. In Case 4β, the scattering gets rapidly weak at 3.5 km (i.e., thin intense scattering). Case 4γ keeps the intense scattering layer down to 10 km, then rapidly turns into a more consolidated structure below that depth.

The simulation results are displayed in Figures 8b–8d. Looking at the vertical components, there is little difference between the three cases. On the other hand, some differences are observed in the horizontal components. For example, while the rise-times of Case 4β and γ (blue and green) coincide with the data within the error bars, the transverse component of Case 4α (red) does not. From the comparison between Case 4α with the rest of the two, it does not seem that the gradually changing structure is suitable for the Apollo 12 landing site.

Concerning the preference between the thin (Case 4β) and the thick scattering layer (Case 4γ), Case 4γ is more similar to the observation, which can be confirmed from the averaged amplitude ratio in Figure 9. In fact, Case 4γ also works well for Apollo 16 SIVB impact (Figure 10). Thus, the intense scattering appears to continue down to 10 km at least at the Apollo 12 landing site.

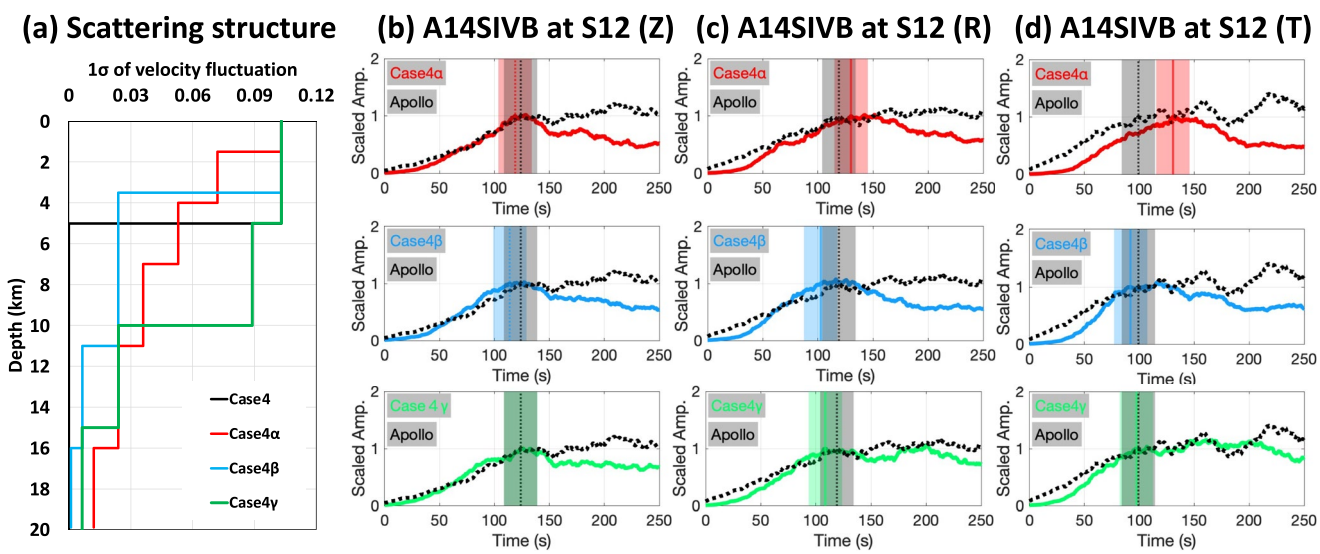

Figure 8. (a) Assumed scattering structures. The black line is Case 4 which was used in the previous section. The red, blue, and green are Case 4α, β, γ, respectively. (b)–(d) The comparisons between the simulation results (colored) with the Apollo data (black) for the vertical, radial, and transverse components from left to right. The first row is for Case 4α, followed by Case 4β, and Case 4γ. The vertical lines with shade represent the rise-times with their error ranges.

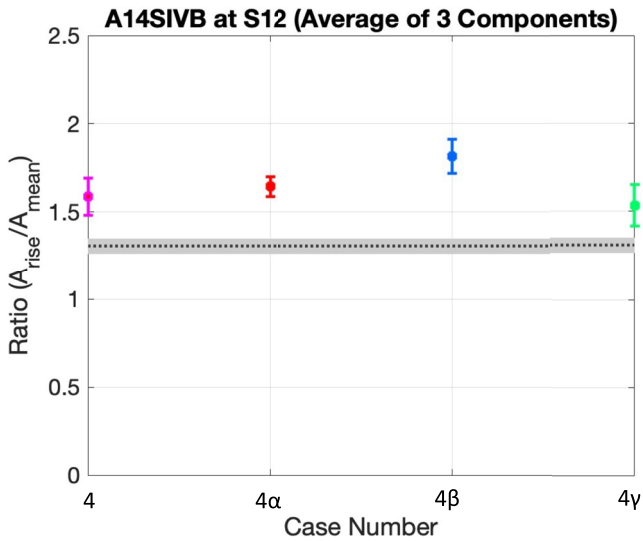

Figure 9. Averaged amplitude ratios of the three components (radial, transverse, and vertical). Magenta plot is for Case 4, red for Case 4α, blue for Case 4β, and green for Case 4γ.

4. Discussion

4.1. Interpretation of the Derived Structure

From the forward modeling, we found that the 10-km intense scattering model (Case 4γ) best explains the observations. The structural transition at 10 km depth was actually expected in previously proposed models (Hawke et al., 2003; Yamamoto et al., 2012), although that is more related to the compositional transition from the mafic-rich materials into the plagioclase-rich anorthosite. It is also pointed out that the mafic-rich layer has compositional variations due to the continuous meteoroid impacts in the early history of the Moon (Hawke et al., 2003). From another aspect, the numerical simulation of the spatial development of impact fragments by Wiggins et al. (2019) showed that the fragmentations with several hundreds of meters—which affect the seismic wave propagation—could develop down to 5 km from the surface. Putting together these pieces of information with our model, within the 10-km scattering layer, the first several-km layer reflects the structural fragmentation and the following layer more reflects the compositional variations; then the structure turns into a massive plagioclase-rich crust at around 10 km depths where the composition and physical structure get more homogeneous.

4.2. Comparison Between the Earth, Mars, and the Moon in Terms of Scattering and Attenuation Environment

The quantified scattering parameter enables us to compare the scattering environment between the Earth, Mars, and the Moon. Figure 11a compares

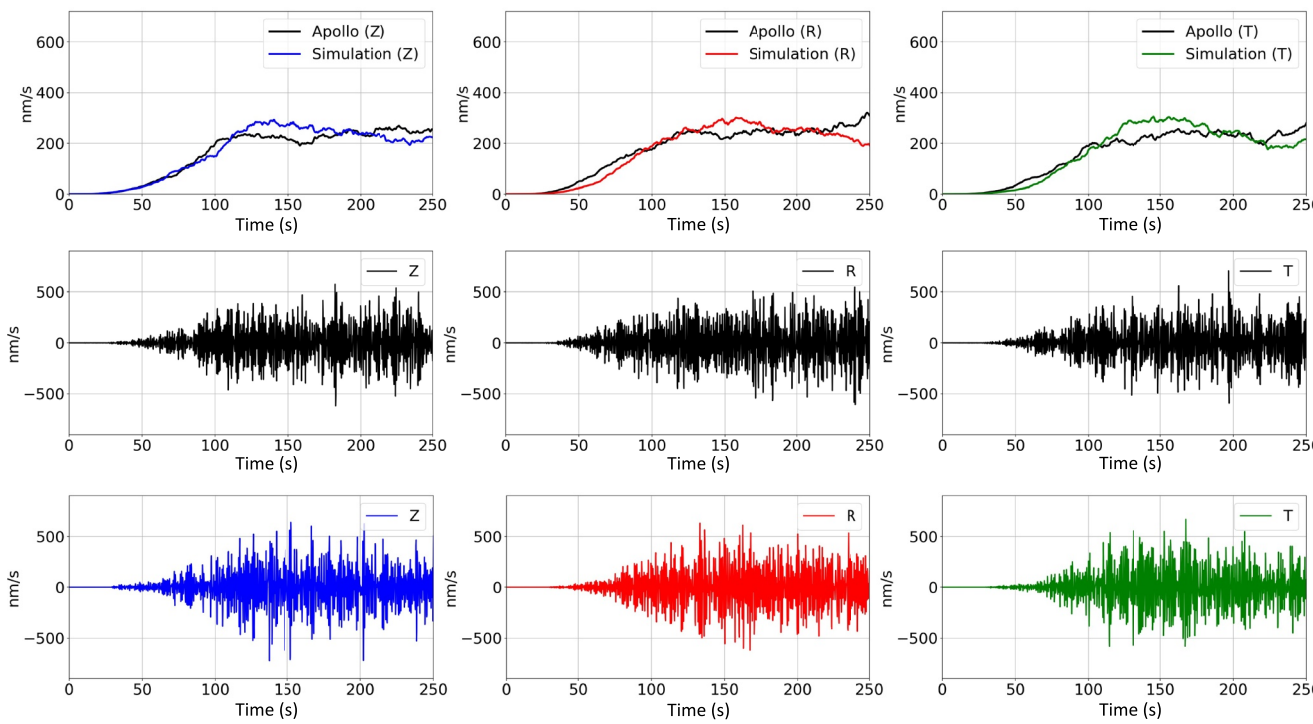

Figure 10. The results for Apollo 16 SIVB impact for Case 4 γ. (Top row) Comparisons of smoothed envelopes between the Apollo (black) and the simulation (colored). (Middle row) The vertical, radial, and transverse waveforms of the Apollo data from the left to right. The waveforms are filtered between 0.3 and 1.5 Hz. (Bottom row) Simulated waveforms in nm/s. The vertical, radial, and transverse components are shown from the left to right. The waveforms are filtered between 0.3 and 1.5 Hz.

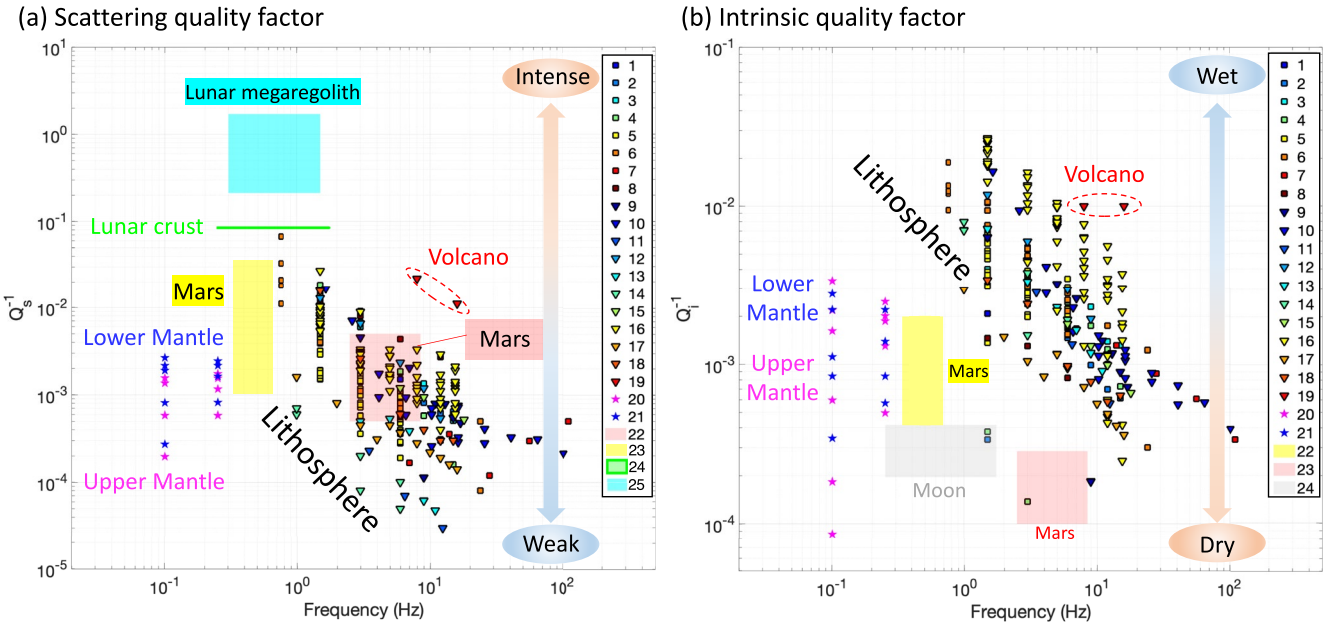

Figure 11. (a) Comparison of scattering attenuation factor between the Earth, Mars, and the Moon. The horizontal axis shows frequency and the vertical shows the inverse value of the scattering attenuation factor. The larger Q_s^{-1} shows the more intense scattering. For the terrestrial case, results for a variety of areas are plotted. The red and yellow hatched areas are the first results of Elysium Planitia on Mars in the InSight mission. The green-filled area shows the previous estimate for the lunar crust and the cyan area shows our result for the lunar megaregolith. The numbers in the legend correspond to the references summarized in Table S6 in Supporting Information S1. (b) Comparison of intrinsic attenuation factor between the Earth, Mars, and the Moon. The larger Q_i^{-1} shows the larger attenuation, implying that the medium holds more fluid. As in (a), the results for various fields on the Earth and Elysium Planitia on Mars, the crust, and/or mantle of the Moon are shown together. The numbers in the legend correspond to the references summarized in Table S7 in Supporting Information S1.

the three solid bodies from the viewpoint of seismic scattering, where the intensity of scattering is evaluated with scattering attenuation factor Q_s defined as follows:

$$Q_s^{-1} = \frac{n_s}{k_s} \tag{8}$$

where, n_s is the scattering coefficient corresponding to the reciprocal of the mean free path between scattering media. Here, we regarded the correlation length as the mean free path. k_s is wavenumber for a given frequency, that is,

$$k_s = \frac{2\pi f}{V} \tag{9}$$

where, f refers to the frequency—ranging from 0.3 to 1.5 Hz—and V is the seismic wave velocity (S-wave velocity in the megaregolith layer in this study). The smaller Q_s value (i.e., larger Q_s^{-1}) means more intense scattering. In Figure 11a, the lunar and Martian Q_s (colored filled area) are superposed on those evaluated at various sites on the Earth (Sato et al., 2012 and references therein).

Paying attention to the terrestrial Q_s^{-1}, it ranges from 10^{-1} to 10^{-5} in the lithosphere and does from 5×10^{-3} to 10^{-4} in the mantle. The volcanic region, whose subsurface structure is heterogeneous, shows a relatively high value of 10^{-2} compared to the typical values for the lithosphere. Turning to Mars, the first results from the InSight (Interior Exploration using Seismic Investigations, Geodesy and Heat Transport) mission (Lognonné et al., 2020; Menina et al., 2021) show a similar value to those observed in the terrestrial lithosphere. Two filled areas are displayed for the Moon: one is estimated based on the radiative transfer modeling (Gillet et al., 2017) and the other is through our numerical simulation. Gillet et al. (2017) analyzed various types of moonquakes besides meteoroid impacts, whose excited waves are sensitive to the subsurface heterogeneity, and estimated the global structure of Q_s (the crustal value is presented in Figure 11a). On the other hand, our research focuses on the closely located impacts, which are suitable for investigating megaregolith—the most heterogeneous region on the Moon. While the lunar crustal Q_s^{-1} is comparable with the most inhomogeneous region on the Earth displayed,

the lunar megaregolith Q_s^{-1} shows a higher value than those measured on the Earth and Elysium Planitia on Mars, suggesting the uppermost part of the Moon is highly heterogeneous.

From our results arise a question; why does the Moon show more intense scattering than others? The answer can be explained by the difference in gravity conditions. It is known that the compressional pressure increases more rapidly under larger gravity conditions. In other words, the critical depth—where the plastic deformation stops—is located shallower as the planet's size gets larger, making it harder for impact fragments to develop (Wiggins et al., 2019). In addition, the existence of an atmosphere plays an important role in the surface evolution of a solid body. With an atmosphere, the impact velocity would be decelerated, resulting in smaller impact energy. Thus, it is reasonable that the Moon has a much more heterogeneous structure because of its small size and the lack of an air shield against continuous meteoroid impacts over several billion years.

Another comparison is made in Figure 11b where the intrinsic attenuation factor Q_i is compared between the three bodies. The smaller Q_i (i.e., larger Q_i^{-1}) indicates that the seismic energy attenuates more rapidly, generally implying that the medium includes more fluid. On Earth, large Q_i^{-1} ($\sim 10^{-2}$) is obtained at geologically active regions (e.g., volcanic front and active fault) (e.g., Sato et al., 2012). In the case of the Moon and Mars, much lower Q_i^{-1} values are obtained, indicating they are in an extremely dry environment, especially compared to the terrestrial lithosphere. This is consistent with the general view of the respective planetary environments. Combining these facts with Q_s results makes it easier to interpret the differences in the seismic observations on each body. Since the Moon is in extremely heterogeneous and low attenuation conditions, the seismic waves are highly scattered with less absorption, making the seismic phases unclear and prolonging the event duration. Mars shows a dry environment, but the scattering factor is comparable with that of the Earth's lithosphere. This explains why marsquakes have a longer duration than those on Earth with less diffused phase arrivals (such as P and S) than moonquakes (Lognonné et al., 2020).

5. Conclusions

In this study, we accomplished the first reproduction of the intensely scattered seismic waves observed on the Moon through the full 3D seismic wave propagation simulation. This allowed us to make significant progress in understandings of scattering properties of the most heterogeneous region of the Moon (megaregolith), which has been a long-standing problem since lunar seismology started.

The quantified scattering parameters are compared with those evaluated on other planets, helping us interpret the different characteristics observed in seismic waves on each solid body. Since the seismic scattering is a common feature seen in planetary seismology, our approach would be helpful in investigating any other solid planetary bodies in future explorations.

To summarize, our study not only just shed light on one of the most complicated problems in lunar seismology but also opened a new way for comparative planetology in terms of seismic scattering, which is expected to give us a paramount key to further understanding of how a planetary surface evolved since its formation.

Acknowledgments
We appreciate Japan Agency for Marine-Earth Science and Technology (JAMSTEC) for providing us with computational resources (the Earth Simulator). We thank Dr. Makiko Ohtake of University of Aizu and Dr. Hiroshi Nagaoka of RIKEN for giving us constructive advice from the viewpoint of the geochemical evolution of the Moon. We acknowledge NASA, CNES, their partner agencies and Institutions (UKSA, SSO, DLR, JPL, IPGP-CNRS, ETHZ, IC, MPS-MPG) and the flight operations team at JPL, SISMOC, MSDS, IRIS-DMC, and PDS for providing SEED SEIS data. We also would like to show our gratitude to editor Laurent Montési and two reviewers for their constructive comments on our manuscript, which helped us make our results and conclusions more solid. This work was supported in part by The Graduate University for Advanced Studies, SOKENDAI.

Data Availability Statement

The Apollo seismic data used in this study were collected from the Data Archives and Transmission System (DARTS) by the Center for Science-satellite Operation and Data Archive (C-SODA) of the Institute of Space and Astronautical Science of the Japan Aerospace Exploration Agency (https://darts.isas.jaxa.jp/planet/seismology/apollo/index.html). Simulation outputs are available at Onodera (2022). The simulation source code (OpenSWPC) is provided by Maeda et al. (2017) available at Maeda (2020). The maps were made with the Generic Mapping Tool (GMT; Wessel et al., 2019). The InSight seismic data used in this study can be retrieved through InSight Mars SEIS data Service (2019).

References

Aki, K. (1969). Analysis of seismic coda of local earthquakes as scattered waves. *Journal of Geophysical Research*, *74*(2), 615–631. https://doi.org/10.1029/jb074i002p00615

Aki, K., & Chouet, B. (1975). Origin of coda waves: Source, attenuation and scattering effect. *Journal of Geophysical Research*, *80*(23), 3322–3342. https://doi.org/10.1029/jb080i023p03322

Araki, H., Tazawa, S., Noda, H., Ishihara, Y., Goossens, S., Sasaki, S., et al. (2009). Lunar global shape and polar topography derived from Kaguya-LALT laser altimetry. *Science*, *323*(5916), 897–900. https://doi.org/10.1126/science.1164146

Barker, M. K., Mazarico, E., Neumann, G. A., Zuber, M. T., Haruyama, J., & Smith, D. E. (2016). A new lunar digital elevation model from the lunar orbiter laser altimeter and SELENE terrain camera. *Icarus*, *273*, 346–355. https://doi.org/10.1016/j.icarus.2015.07.039

Besserer, J., Nimmo, F., Wieczorek, M. A., Weber, R. C., Kiefer, W. S., McGovern, P. J., et al. (2014). GRAIL gravity constraints on the vertical and lateral density structure of the lunar crust. *Geophysical Research Letters*, *41*(16), 5771–5777. https://doi.org/10.1002/2014GL060240

Blanchette-Guertin, J.-F., Johnson, C. L., & Lawrence, J. F. (2012). Investigation of scattering in lunar seismic coda. *Journal of Geophysical Research*, *117*(E6), E06003. https://doi.org/10.1029/2011JE004042

Blanchette-Guertin, J. F., Johnson, C. L., & Lawrence, J. F. (2015). Modeling seismic energy propagation in highly scattering environments. *Journal of Geophysical Research: Planets*, *120*(3), 515–537. https://doi.org/10.1002/2014JE004654

Dainty, A. M., & Toksöz, M. N. (1981). Seismic coda on the Earth and the Moon: A comparison. *Physics of the Earth and Planetary Interiors*, *26*, 250–260. https://doi.org/10.1016/0031-9201(81)90029-7

Dainty, A. M., Toksöz, M. N., Anderson, K. R., Pines, P. J., Nakamura, Y., & Latham, G. (1974). Seismic scattering and shallow structure of the Moon in Oceanus Procellarum. *The Moon*, *9*(1–2), 11–29. https://doi.org/10.1007/bf00565388

Daubar, I. J., Lognonné, P., Teanby, N. A., Collins, G. S., Clinton, J., Stahler, S., et al. (2020). A new crater near InSight: Implications for seismic impact detectability on Mars. *Journal of Geophysical Research: Planets*, *125*(8), e2020JE006382. https://doi.org/10.1029/2020JE006382

Gagnepain-Beyneix, J., Lognonné, P., Chenet, H., Lombardi, D., & Spohn, T. (2006). A seismic model of the lunar mantle and constraints on temperature and mineralogy. *Physics of the Earth and Planetary Interiors*, *159*, 140–166.

Garcia, R. F., Gagnepain-Beyneix, J., Chevrot, S., & Lognonné, P. (2011). Very preliminary reference Moon model. *Physics of the Earth and Planetary Interiors*, *188*(1–2), 96–113. https://doi.org/10.1016/j.pepi.2011.06.015

Garcia, R. F., Khan, A., Drilleau, M., Margerin, L., Kawamura, T., Sun, D., et al. (2019). Lunar seismology: An update on interior structure models. *Space Science Reviews*, *215*(8), 50. https://doi.org/10.1007/s11214-019-0613-y

Gillet, K., Margerin, L., Calvet, M., & Monnereau, M. (2017). Scattering attenuation profile of the Moon: Implications for shallow moonquakes and the structure of the megaregolith. *Physics of the Earth and Planetary Interiors*, *262*, 28–40. https://doi.org/10.1016/j.pepi.2016.11.001

Hawke, B. R., Peterson, C. A., Blewett, D. T., Bussey, D. B. J., Lucey, P. G., Taylor, G. J., & Spudis, P. D. (2003). Distribution and modes of occurrence of lunar anorthosite. *Journal of Geophysical Research*, *108*, 5050. https://doi.org/10.1029/2002JE001890,E6

InSight Mars SEIS data Service. (2019). SEIS raw data, InSight mission. IPGP, JPL, CNES, ETHZ, ICL, MPS, ISAE-Supaero, LPG, MSFC. https://doi.org/10.18715/SEIS.INSIGHT.XB_2016

Karakostas, F., Schmerr, N., Maguire, R., Huang, Q., Kim, Q., Lekic, V., et al. (2021). Scattering attenuation of the Martian interior through coda-wave analysis. *Bulletin of the Seismological Society of America*, *111*(6), 3035–3054. https://doi.org/10.1785/0120210253

Latham, G., Ewing, M., Dorman, J., Press, F., Toksoz, N., Sutton, G., et al. (1970). Seismic data from man-made impacts on the Moon. *Science*, *170*(3958), 620–626. https://doi.org/10.1126/science.170.3958.620

Lognonné, P., Banerdt, W. B., Pike, W. T., Giardini, D., Christensen, U., Garcia, R. F., et al. (2020). Constraints on the shallow elastic and anelastic structure of Mars from InSight seismic data. *Nature Geoscience*, *13*(3), 213–220. https://doi.org/10.1038/s41561-020-0536-y

Lognonné, P., Gagnepain-Beyneix, J., & Chenet, H. (2003). A new seismic model of the Moon: Implications for structure, thermal evolution and formation of the Moon. *Earth and Planetary Science Letters*, *211*(1–2), 27–44. https://doi.org/10.1016/S0012-821X(03)00172-9

Maeda, T. (2020). tktmyd/OpenSWPC: Version 5.1.0. *Zenodo*. https://doi.org/10.5281/zenodo.3982232

Maeda, T., Takemura, S., & Furumura, T. (2017). OpenSWPC: An open-source integrated parallel simulation code for modeling seismic wave propagation in 3D heterogeneous viscoelastic media. *Earth Planets and Space*, *69*(1), 102. https://doi.org/10.1186/s40623-017-0687-2

Menina, S., Margerin, L., Kawamura, T., Lognonné, P., Marti, J., Drilleau, M., et al. (2021). Energy envelope and attenuation characteristics of high frequency (HF) and very-high-frequency (VF) Martian events. *Bulletin of the Seismological Society of America*, *111*(6), 3016–3034. https://doi.org/10.1785/0120210127

Mizutani, H., & Osako, M. (1974). Elastic-wave velocities and thermal diffusivities of Apollo 17 rocks and their geophysical implications. In *Lunar and Planetary Science Conference Proceedings* (Vol. *5*, pp. 2891–2901).

Nakamura, T., Takenaka, H., Okamoto, T., & Kaneda, Y. (2012). FDM simulation of seismic-wave prop-agation for an aftershock of the 2009 Suruga Bay earthquake: Effects of ocean-bottom topography and seawater layer. *Bulletin of the Seismological Society of America*, *102*(6), 2420–2435. https://doi.org/10.1785/0120110356

Nakamura, Y., & Koyama, J. (1982). Seismic *Q* of the lunar upper mantle. *Journal of Geophysical Research*, *87*(B6), 4855–4861. https://doi.org/10.1029/JB087iB06p04855

Oberst, P. J. (1989). *Meteoroids near the Earth-Moon system as inferred from temporal and spatial distribution of impacts detected by the lunar seismic network*, PhD dissertation. The University of Texas at Austin.

Onodera, K. (2022). Onodera0726/JGR_Onodera_2022. *GitHub Data Repository*. https://doi.org/10.5281/zenodo.7151401

Onodera, K., Kawamura, T., Tanaka, S., Ishihara, Y., & Maeda, T. (2021). Numerical simulation of lunar seismic wave propagation: Investigation of subsurface scattering properties near Apollo 12 landing site. *Journal of Geophysical Research: Planets*, *126*(3), e2020JE006406. https://doi.org/10.1029/2020JE006406

Rajšić, A., Miljković, K., Wójcicka, N., Collins, G. S., Onodera, K., Kawamura, T., et al. (2021). Numerical simulations of the Apollo S-IVB artificial impacts on the Moon. *Earth and Space Science*, *8*(12), e2021EA001887. https://doi.org/10.1029/2021EA001887

Sato, H. (1977). Energy propagation including scattering effect. Single isotropic scattering approximation. *Journal of Physics of the Earth*, *25*(1), 27–41. https://doi.org/10.4294/jpe1952.25.27

Sato, H., & Fehler, M. (1998). *Seismic wave propagation and scattering in the heterogeneous Earth*. AIP Press/Springer.

Sato, H., Fehler, M. C., & Maeda, T. (2012). *Seismic wave propagation and scattering in the heterogeneous Earth* (2nd ed.). Springer.

Shiomi, K., Sato, H., & Ohtake, M. (1997). Broad-band power-law spectra of well-log data in Japan. *Geophysical Journal International*, *130*(1), 57–64. https://doi.org/10.1111/j.1365-246X.1997.tb00987.x

Sivaji, C., Nishizawa, O., Kitagawa, G., & Fukushima, Y. (2002). Aphysical-model study of the statistics of seismic waveform fluctuations in random heterogeneous media. *Geophysical Journal International*, *148*(3), 575–595. https://doi.org/10.1046/j.1365-246x.2002.01606.x

Sondergeld, C. H., Granryd, L. A., & Spetzler, H. A. (1979). Compressional velocity measurements for a highly fractured lunar anorthosite. *Proceedings of the Lunar and Planetary Science Conference*, *10*, 2147–2154.

Suzuki, H., Ikeda, R., Mikoshiba, T., Kinoshita, S., Sato, H., & Takahashi, H. (1981). Deep well logs in the Kanto-Tokai area (in Japanese). *Review of Research for Disaster Prevention, National Research Center for Disaster Prevention*, *65*, 1–162.

Teanby, N., & Wookey, J. (2011). Seismic detection of meteorite impacts on Mars. *Physics of the Earth and Planetary Interiors*, *186*(1–2), 70–80. https://doi.org/10.1016/j.pepi.2011.03.004

Wessel, P., Luis, J. F., Uieda, L., Scharroo, R., Wobbe, F., Smith, W. H. F., & Tian, D. (2019). The generic mapping tools version 6. *Geochemistry, Geophysics, Geosystems*, *20*(11), 5556–5564. https://doi.org/10.1029/2019GC008515

Wieczorek, M. A., Neumann, G. A., Nimmo, F., Kiefer, W. R., Taylor, G. J., Melosh, H. J., et al. (2013). The crust of the Moon as seen by GRAIL. *Science*, *339*(6120), 671–675. https://doi.org/10.1126/science.1231530

Wiggins, S. E., Johnson, B. C., Bowling, T. J., Melosh, H. J., & Silber, E. A. (2019). Impact fragmentation and the development of the deep lunar megaregolith. *Journal of Geophysical Research: Planets*, *124*(4), 941–957. https://doi.org/10.1029/2018JE005757

Wu, R. S., & Aki, K. (1985). Multiple scattering and energy transfer of seismic waves—Separation of scattering effect from intrinsic attenuation—II. Application of the theory to Hindu-Kush region. *Pure and Applied Geophysics*, *128*(1–2), 49–80. https://doi.org/10.1007/bf01772590

Yamamoto, S., Nakamura, R., Matsunaga, T., Ogawa, Y., Ishihara, Y., Morota, T., et al. (2012). Massive layer of pure anorthosite on the Moon. *Geophysical Research Letters*, *39*(13), L13201. https://doi.org/10.1029/2012GL052098

Zhang, W., & Shen, Y. (2010). Unsplit complex frequency-shifted PML implementation using auxiliary differential equations for seismic wave modeling. *Geophysics*, *75*(4), T141–T154. https://doi.org/10.1190/1.3463431

References From the Supporting Information

Adams, D. A., & Abercrombie, R. E. (1998). Seismic attenuation above 10 Hz in southern California from coda waves recorded in the Cajon Pass borehole. *Journal of Geophysical Research*, *103*(B10), 24257–24270. https://doi.org/10.1029/98JB01757

Akinci, A., & Eyidogan, H. (2000). Scattering and anelastic attenuation of seismic energy in the vicinity of north Anatolian fault zone, eastern Turkey. *Physics of the Earth and Planetary Interiors*, *122*(3–4), 229–239. https://doi.org/10.1016/S0031-9201(00)00196-5

Akinci, A., Pezzo, E. D., & Ibanez, J. M. (1995). Separation of scattering and intrinsic attenuation in southern Spain and western Anatolia (Turkey). *Geophysical Journal International*, *121*(2), 337–353. https://doi.org/10.1111/j.1365-246X.1995.tb05715.x

Bianco, F., Pezzo, E. D., Castellano, M., Ibanez, J., & Luccio, F. D. (2002). Separation of intrinsic and scat-tering seismic attenuation in the Southern Apennine zone, Italy. *Geophysical Journal International*, *150*(1), 10–22. https://doi.org/10.1046/j.1365-246X.2002.01696.x

Bianco, F., Pezzo, E. D., Malagnini, L., Luccio, F. D., & Akinci, A. (2005). Separation of depth-dependent intrinsic and scattering seismic attenuation in the northeastern sector of the Italian Peninsula. *Geophysical Journal International*, *161*(1), 130–142. https://doi.org/10.1111/j.1365-246X.2005.02555.x

Dutta, U., Biswas, N., Adams, D., & Papageorgiou, A. (2004). Analysis of S-wave attenuation in South- central Alaska. *Bulletin of the Seismological Society of America*, *94*(1), 16–28. https://doi.org/10.1785/0120030072

Fehler, M., Hoshiba, M., Sato, H., & Obara, K. (1992). Separation of scattering and intrinsic attenuation for the Kanto-Tokai region, Japan, using measurements of S-wave energy versus hypocentral distance. *Geophysical Journal International*, *108*(3), 787–800. https://doi.org/10.1111/j.1365-246X.1992.tb03470.x

Giampiccolo, E., Tuve, T., Gresta, S., & Patane, D. (2006). S-waves attenuation and separation of scattering and intrinsic absorption of seismic energy in southeastern Sicily (Italy). *Geophysical Journal International*, *165*(1), 211–222. https://doi.org/10.1111/j.1365-246X.2006.02881.x

Goutbeek, F. H., Dost, B., & van Eck, T. (2004). Intrinsic absorption and scattering attenuation in the southern part of The Netherlands. *Journal of Seismology*, *8*(1), 11–23. https://doi.org/10.1023/B:JOSE.0000009511.27033.79

Gudkova, T. V., Lognonné, P., & Gagnepain-Beyneix, J. (2011). Large impacts detected by the Apollo seismometers: Impactor mass and source cutoff frequency estimations. *Icarus*, *211*(2), 1049–1065. https://doi.org/10.1016/j.icarus.2010.10.028

Gudkova, T. V., Lognonné, P., Miljković, K., & Gagnepain-Beyneix, J. (2015). Impact cutoff frequency—Momentum scaling law inverted from Apollo seismic data. *Earth and Planetary Science Letters*, *427*, 57–65. https://doi.org/10.1016/j.epsl.2015.06.037

Hatzidimitriou, P. M. (1994). Scattering and anelastic attenuation of seismic energy in northern Greece. *Pure and Applied Geophysics*, *143*(4), 587–601. https://doi.org/10.1007/BF00879499

Hoshiba, M. (1993). Separation of scattering attenuation and intrinsic absorption in Japan using the multiple lapse time window analysis of full seismogram envelope. *Journal of Geophysical Research*, *98*(B9), 15809–15824. https://doi.org/10.1029/93JB00347

Jin, A., Mayeda, K., Adams, D., & Aki, K. (1994). Separation of intrinsic and scattering attenuation in southern California using TERRAscope data. *Journal of Geophysical Research*, *99*(B9), 17835–17848. https://doi.org/10.1029/94JB01468

Leary, P., & Abercrombie, R. (1994). Frequency dependent crustal scattering and absorption at 5−160 Hz from coda decay observed at 2.5 km depth. *Geophysical Research Letters*, *21*(11), 971–974. https://doi.org/10.1029/94GL00977

Lee, W. S., Sato, H., & Lee, K. (2003). Estimation of *S*-wave scattering coefficient in the mantle from envelope characteristics before and after the *ScS* arrival. *Geophysical Research Letters*, *30*(24), 2248. https://doi.org/10.1029/2003GL018413

Lee, W. S., Sato, H., & Lee, K. (2006). Scattering coefficients in the mantle revealed from the seismogram envelope analysis based on the multiple isotropic scattering model. *Earth and Planetary Science Letters*, *241*(3–4), 888–900. https://doi.org/10.1016/j.epsl.2005.10.035

Mayeda, K., Koyanagi, S., Hoshiba, M., Aki, K., & Zeng, Y. (1992). A comparative study of scattering, intrinsic, and coda Q^{-1} for Hawaii, Long Valley, and central California between 1.5 and 15.0 Hz. *Journal of Geophysical Research*, *97*(B5), 6643–6659. https://doi.org/10.1029/91JB03094

Orloff (2000). Apollo by the numbers: A statistical reference. NASA SP-2000-4029.

Toksöz, M. N., Dainty, A. M., Solomon, S. C., & Anderson, K. R. (1974). Structure of the Moon. *Reviews of Geophysics*, *12*(4), 539–567. https://doi.org/10.1029/RG012i004p00539

Ugalde, A., Pujades, L. G., Canas, J. A., & Villasenor, A. (1998). Estimation of the intrinsic absorption and scattering attenuation in northeastern Venezuela (southeastern Caribbean) using coda waves. *Pure and Applied Geophysics*, *153*, 685–702. https://doi.org/10.1007/978-3-0348-8711-3_21

Vargas, C. A., Ugalde, A., Pujades, L. G., & Canas, J. A. (2004). Spatial variation of coda wave attenuation in northwestern Colombia. *Geophysical Journal International*, *158*(2), 609–624. https://doi.org/10.1111/j.1365-246X.2004.02307.x

Yamamoto, M., & Sato, H. (2010). Multiple scattering and mode conversion revealed by an active seismic experiment at Asama volcano, Japan. *Journal of Geophysical Research*, *115*(B7), B07304. https://doi.org/10.1029/2009JB007109

Wagner, R. V., Nelson, D. M., Plescoa, J. B., Robinson, M. S., Speyerer, E. J., & Mazarico, E. (2017). Coordinates of anthoropogenic features on the Moon. *Icarus*, *283*, 92–103. https://doi.org/10.1016/j.icarus.2016.05.011